J. Fluid Mech. (2011), *vol.* 682, *pp.* 241–260. © Cambridge University Press 2011
doi:10.1017/jfm.2011.212

Cavitation bubble dynamics in a liquid gap of variable height

SILVESTRE ROBERTO GONZALEZ-AVILA[1], EVERT KLASEBOER[2], BOO CHEONG KHOO[3] AND CLAUS-DIETER OHL[1]†

[1]Nanyang Technological University, School of Physical and Mathematical Sciences, Division of Physics and Applied Physics, 21 Nanyang Link, Singapore 637371

[2]Institute of High Performance Computing, Fusionopolis, 1 Fusionopolis Way, 16–16 Connexis, Singapore 138632

[3]Department of Mechanical Engineering, National University of Singapore, 10 Kent Ridge Crescent, Singapore 119260

(Received 2 November 2010; revised 24 April 2011; accepted 8 May 2011; first published online 21 June 2011)

We report on an experimental study of cavitation bubble dynamics within sub-millimetre-sized narrow gaps. The gap height is varied, while the position of the cavitation event is fixed with respect to the lower gap wall. Four different sizes of laser-induced cavitation bubbles are studied using high-speed photography of up to 430,000 frames per second. We find a strong influence of the gap height, H, on the bubble dynamics, in particular on the collapse scenario. Also, similar bubble dynamics was found for the same non-dimensional gap height $\eta = H/R_x$, where R_x is the maximum radius in the horizontal direction. Three scenarios are observed: neutral collapse at the gap centre, collapse onto the lower wall and collapse onto the upper wall. For intermediate gap height the bubble obtains a conical shape $1.4 < \eta < 7.0$. For large distances, $\eta > 7.0$, the bubble no longer feels the presence of the upper wall and collapses hemispherically. The collapse time increases with respect to the expansion time for decreasing values of η. Due to the small scales involved, the final stage of the bubble collapse could not be resolved temporally and numerical simulations were performed to elucidate the details of the flow. The simulations demonstrate high-speed jetting towards the upper and lower walls and complex bubble splitting for neutral collapses.

Key words: bubble dynamics, cavitation, microfluidics

1. Introduction

Cavitation, the formation of largely empty voids in liquids, is studied now for more than a century (Reynolds 1886) mainly because of its damaging effect of all known material surfaces. Cavitation damage has been observed for example on ship propellers, rudders and turbine blades.

Cavitation is also found when two rigid interfaces submerged in a liquid which are initially in contact are pulled apart (Chen & Israelachvili 1991). Here, cavitation occurs in a narrow gap and may lead to damage of the contacting interfaces in ball-bearings

† Email address for correspondence: cdohl@ntu.edu.sg

https://doi.org/10.1017/jfm.2011.212 Published online by Cambridge University Press

and similar devices. Reynolds remarked that 'the pressure would become negative if the condition did not break down by discontinuity in the oil, which is sure to occur when the pressure falls below that of zero'.

Another application where cavitation is affected by narrow geometries is ultrasonic cleaning. Here, the bubble activity creates strong shear forces which enable the detachment of surface adherent contamination (Krefting, Mettin & Lauterborn 2004; Kim *et al.* 2009). Surfaces encountered in ultrasonic cleaning applications possess complex shapes, such as assembled electronic boards, surgical instruments and the ridges and trenches of memory chips. What these surfaces have in common is that the bubble dynamics takes place within narrow gaps to remove the attached dirt. Very limited knowledge exists concerning the effect of multiple rigid boundaries on the bubble dynamics.

In the past, several numerical studies have been conducted regarding bubbles between two parallel plates. Ishida *et al.* (2001) used a boundary element method to simulate the behaviour of initially spherical bubbles between two solid boundaries. The normalized stand-off parameter in these studies was relatively large with $\gamma \approx 1$. In contrast, Shima & Nakajima (1977) used a perturbation approach to study the evolution of an approximately hemispherical bubble near a solid boundary; although limited by their approach they found that the bubble shape during the collapse phase depends strongly on the bubble's initial deformation. Experimental results from Chahine (1982), Ishida *et al.* (2001) and Kucherenko & Shamko (1986) show the splitting of bubbles during collapse; these studies are done only for a stand-off parameter of around 1. Kucherenko & Shamko (1986) reported bubbles created at $\gamma < 1$; however, not many frames are available that describe the bubble shape during its collapse. Quinto-Su, Lim & Ohl (2009) investigated the effect of the bubble collapse time as a function of gap height using high-speed photography. However, they visualized the bubbles through the transparent boundary and thus cannot resolve the shape of the bubble in greater detail. However, they observed a toroidal bubble shape during collapse which was explained with jetting.

Cavitation dynamics in narrow gaps is also of interest for microfluidic applications. There, cavitation bubbles are created in thin channels with the help of laser pulses to pump and mix fluids (Dijkink & Ohl 2008) or to manipulate rigid objects (Quinto-Su *et al.* 2010) or cells (Ohl *et al.* 2006; Le Gac *et al.* 2007). The height of the microfluidic channel is an important parameter influencing the liquid flow and in particular the jetting dynamics.

So far, most studies (if not all) on cavitation in these narrow gaps observed the bubble dynamics through the transparent boundary; thus, it was not possible to resolve the bubble dynamics normal to the boundaries. Yet, jetting dynamics, which may cause material erosion and/or enhance cleaning, should also be studied from a side view. Hence, we focus in this study on this view to study bubble translation, shape and the direction of liquid jets; nevertheless, we are limited by the framing rate and experimental constraints and thus cannot resolve jetting velocities and shock wave emission.

2. Experimental set-up

Figure 1 shows a schematic diagram of the experimental set-up to create and photograph a cavitation bubble within a narrow and liquid-filled gap. The bubbles are generated with an expanded and refocused beam from a Q-switched Nd:YAG laser (New Wave Research, wavelength 532 nm, and pulse duration 6 ns), inside a thin

https://doi.org/10.1017/jfm.2011.212 Published online by Cambridge University Press

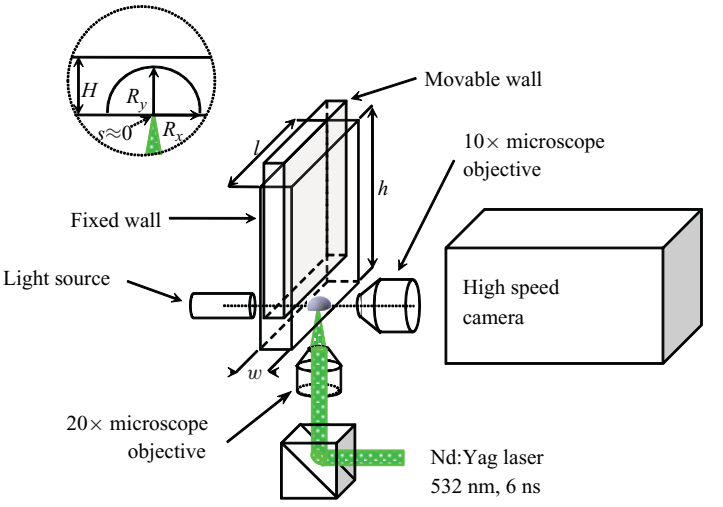


FIGURE 1. (Colour online available at journals.cambridge.org/flm) Experimental set-up to visualize the bubbles in a gap of varying height (not drawn to scale). The bubble is generated by focusing a pulsed laser beam at the bottom of a narrow gap formed by a lower fixed wall and a movable upper wall. The upper left inset depicts the geometric parameters used in this study (see text).

vertical channel (μ-slide, Ibidi Germany) of 5 mm in length (l), 0.6 mm in width (w) and 25 mm in height (h). Inside this channel, a transparent slender column made of polycarbonate of 4 mm $\times$ 0.5 mm $\times$ 40 mm was inserted. The position of this slender column can be adjusted to set the height of the liquid-filled gap. The lower wall is made of a microscope slide glued carefully to the channel. The separation between the lower and the upper walls can be varied from 0 to 10 mm. The bubbles were created in printer ink (yellow, Maxtec universal refill ink, dynamic viscosity $\mu = 1.6 \times 10^{-3}$ Pa s and density $\rho = 996\,\mathrm{kg\,m^{-3}}$). The channel or test section was placed on a custom made microscope table of an inverted microscope, Olympus, IX71, and positioned with a precision three-axis traverse stage. The contact angle between the printer ink and the glass surface is $21 \pm 2^{\circ}$. The laser which is beamed into the inverted microscope is deflected by a dichroic mirror and focused with a 20 $\times$ microscope objective (LCAch N Olympus, Japan) at the centre of the test section very close to the surface of the lower wall so as to produce initially hemispherical bubbles.

A 10 $\times$ microscope objective magnifies the scene and images it onto the sensor of a high-speed camera (Fastcam SA1.1, Photron, Japan) to record the spatial and temporal evolution of the bubbles. To prevent damage to the camera sensor, a notch filter (NF20–532S-25, Semrock, USA) is placed in front of it to block the laser wavelength. For a proper visualization of the bubbles the test section was illuminated from the back with an intense metal halide lamp (ILP-2, Olympus, Japan). The experiments were recorded at frame rates between 250 000 and 432 000 frames per second (f.p.s.) with exposure times between 1.0 and 2.3 µs. The image resolution varied from 128 (H) $\times$ 80 (V) pixels in the experiments for the larger bubbles and down to 64 (H) $\times$ 48 (V) pixels for the smallest bubbles. In all the experiments performed, the resolution was 2.9 µm pixel^{-1}. The upper left inset of figure 1 details the configuration where the bubbles are created; the upper wall is movable, thus allowing the study of the effect of the liquid height, H, on the bubble dynamics.

https://doi.org/10.1017/jfm.2011.212 Published online by Cambridge University Press

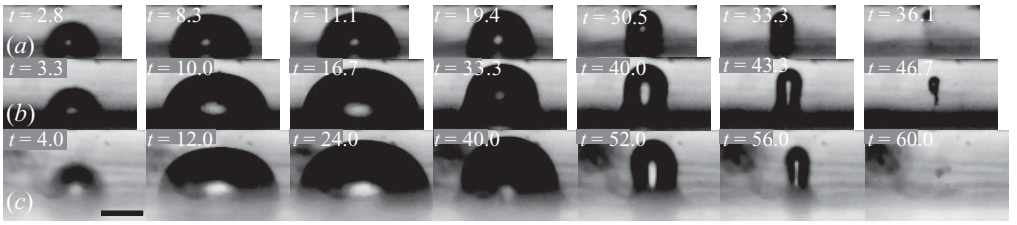


FIGURE 2. Comparison of the observed bubble dynamics with increasing maximum radii but for approximately the same non-dimensional channel height, $\eta = H/R_x = 1.21 \pm 0.03$: (*a*) $R_x = 101\,\mu$m captured at 360 000 f.p.s.; (*b*) $R_x = 141\,\mu$m captured at 300 000 f.p.s.; (*c*) $R_x = 168\,\mu$m captured at 250 000 f.p.s. The time is given in the upper left corner of each frame in microseconds. Frames are selected from the high-speed recordings to show the stages of nucleation, expansion, maximum volume and the collapse (four frames). The horizontal bar in the lower right corner of sequence (*c*) depicts a length of 100 μm. See table 1 for experimental parameters.

At the beginning of the experiments, the test section was positioned in such a way that the bubbles are created at the centre of the test chamber. The camera was positioned next to the test section to visualize the bubble sideways, as shown in figure 1. The camera, the 10 × microscope objective, and the test section are positioned each on a three-axis stage for accurate positioning.

At first, the position of the 20 × microscope was adjusted to produce hemispherical bubbles with the upper boundary positioned far away. This is judged from the ratio of the vertical, R_y, to horizontal radius, R_x, at maximum expansion, i.e. $\alpha = R_y/R_x \approx 1 \pm 0.02$. Once the hemispherical bubbles were obtained the upper wall was moved to a distance of approximately 30 μm from the lower wall. This wall was raised in subsequent experiments.

The bubbles created for this study have a stand-off distance $s \approx 0$, where s is the distance between the bubble centre and the nearest boundary; in the literature (Vogel, Lauterborn & Timm 1989; Tong *et al.* 1999; Lindau & Lauterborn 2003) this corresponds to the non-dimensional parameter $\gamma = s/R_x \approx 0$, see the inset of figure 1. To characterize the dynamics, we make use of three non-dimensional parameters, the dimensionless channel height, $\eta = H/R_x$, the bubble to channel height ratio $\beta = R_y/H$, and the sphericity parameter $\alpha = R_y/R_x$.

3. Experimental results

3.1. *High-speed recording*

Some typical results for different maximum bubble sizes, but similar η values are shown in figure 2; each sequence shows the bubble just after it is created (frame 1), during expansion (frame 2) and at maximum expansion (frame 3); after this, the following three frames show the shrinkage/collapse of the bubble; the last frame of sequences in figures 2(*a*) and 2(*b*) depicts the bubble around the time it reaches its minimum volume; in the last frame of sequence in figure 2(*c*) the bubble has recondensed into the liquid.

We see that the bubble dynamics can be nicely captured with the set-up which allows a thorough study of its dynamics as a function of its maximum volume and the gap height. The size of the bubble is conveniently adjusted by changing the laser energy.

https://doi.org/10.1017/jfm.2011.212 Published online by Cambridge University Press

R_x (μm)	η	t_{osc} (μs)	t_{ec} (μs)	t^*
101	1.19	20.2	37.5 ± 1.4	1.9 ± 0.1
141	1.21	28.2	48.4 ± 1.7	1.7 ± 0.1
168	1.25	33.6	58.0 ± 2.0	1.7 ± 0.1

TABLE 1. Experimental parameters of the cavitation bubbles shown in figure 2.

The above sequences, figure 2(*a–c*), show that despite having different sizes, the bubble dynamics is very similar, that is each bubble collapses approximately in the centre between the upper and the lower walls. Also, for similar η values of around 1.2, we obtain similar non-dimensional collapse times, $t^* = t_{ec}/t_{osc}$. This is defined as the time between the bubble expansion and its collapse, t_{ec}, divided by the oscillation time of a spherical bubble in an infinite medium, i.e. far away from boundaries; thus, $t_{osc} \approx 1.83 R_x(\rho/P)^{1/2}$, where ρ is the liquid density and P is the pressure in the liquid far from the bubble, which we assume $P = 10^5$ Pa.

Table 1 summarizes the experimental values of figure 2. Interestingly, not only the bubbles show a neutral collapse (between the two walls) they also have a very similar non-dimensional collapse time, t^*. This allows collating the experiments with differently sized bubbles into a single graph, as will be shown later.

A representative set of experiments where the gap height is varied while the bubble radius, $R_X \approx 140$ μm, is kept constant is depicted in figure 3. From left to right, the first frame presents the bubble during the expansion phase just 3.3 μs after inception, which due to its fast motion is slightly blurred. Frame 2 shows the bubble during expansion and in frame 3 the bubble has reached its maximum volume. The next three frames depict the bubble during its collapse phase. The last frame shows the state of the bubble after it reached its minimum volume. Here, the non-dimensional gap height is varied between $\eta = 0.4$ and $\eta = 7.3$ (51–1000 μm).

In figure 3(*a*) the bubble expands and contracts almost like a cylindrical disk. Some remnant bubbles can be observed in the last frame, which are equally distributed over the full height of the channel, indicating that the collapse of the bubble was mostly cylindrical. The bubble in figure 3(*b*) expands initially across the lower wall; at maximum expansion the bubble reaches the upper wall, and then it appears to 'stick' to the upper wall where it moves towards during its collapse. Figure 3(*c*) shows a bubble similar to that of figure 3(*b*); however, when the bubble reaches its maximum expansion, the bubble does not reach the upper wall. Nonetheless, the collapse of the bubble proceeds as in figure 3(*b*), that is the bubble collapses onto the upper wall. Figure 3(*d*) depicts a bubble that is contracting rapidly. The change in the shape of the bubble from frame 4 to frame 5 suggests that the lateral walls contract rapidly, which might have caused a split of the bubble between frames 5 and 6. Increasing the distance between the walls the bubble collapses with a cone-like shape on the lower boundary as seen in figure 3(*e*) (frames 5 and 6). For figure 3(*f*) the upper wall is situated quite far from the lower wall and the bubble appears to expand and collapse in an almost hemispherical shape. A total of 90 experiments were conducted, and they all show similar collapse scenarios as those shown in figure 3(*a–f*).

3.2. *Collapse scenarios*

In general, we find five distinct types of bubble collapses which we categorize as disk-shaped collapse, upward jetting, neutral collapse, non-spherical collapse with a conical shape, and a quasi-hemispherical collapse. Interestingly, there seem to be rather

https://doi.org/10.1017/jfm.2011.212 Published online by Cambridge University Press

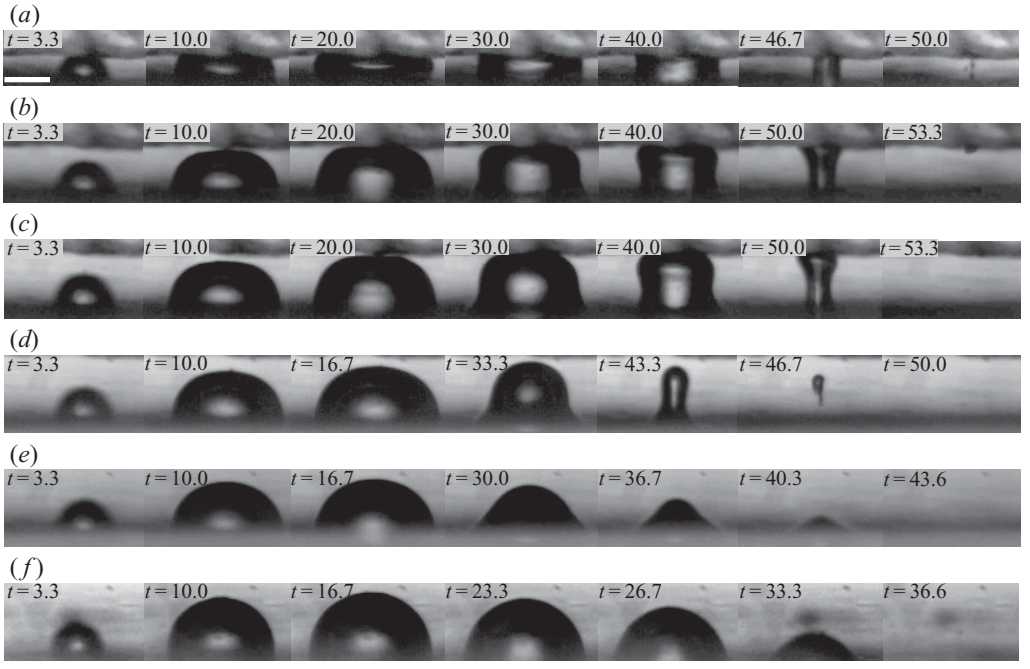


FIGURE 3. Bubble dynamics as a function of channel height for bubbles with an approximate maximum horizontal bubble radius of $R_x = 140\,\mu$m. The upper wall is visible in (*a–d*); the time in microseconds is shown on the upper left corner of each frame. (*a*) $\eta = H/R_x = 0.4$, $\beta = 1.0$, bubble collapse between the two walls; (*b*) $\eta = 0.8$, $\beta = 1.0$, bubble collapse onto the upper wall, at maximum expansion the bubble reaches the upper wall; (*c*) $\eta = 0.9$, $\beta = 0.9$, bubble collapse onto the upper wall, the bubble does not reach the upper wall at maximum expansion; (*d*) $\eta = 1.2$, $\beta = 0.8$, neutral collapse; (*e*) $\eta = 1.6$, $\beta = 0.6$, non-spherical collapse onto the lower wall; and (*f*) $\eta = 7.3$, $\beta = 0.1$, quasi-hemispherical collapse onto the lower wall. The white bar in (*a*) indicates a length of 100 μm.

sharp boundaries between these five different scenarios which we can distinguish with increasing η values ($\eta = H/R_x$). The first boundary of η, $\eta \sim 0.3$ to 0.4, separates the disk-shaped bubble from the upward jetting region. Bubbles with $\eta > 1$ and $\eta < 1.4$ show a neutral collapse with no distinct jetting. For larger η values, the collapse proceeds in contact with the lower wall and we find that for $\eta > 7$ the bubble assumes an almost hemispherical shape during its entire dynamics.

3.2.1. *Disk-shaped bubble*

In this region, the bubble expands and collapses in contact with both walls. A typical example of the time evolution of this type of bubbles can be seen in figure 3(*a*) for $\eta = 0.4$. The bubble expands and except for frame 1, the expansion and collapse of the bubble takes place between the two walls which we find for maximum radii $R_x = 108$, 140 and 170 μm.

3.2.2. *Upward jet*

An interesting change in bubble dynamics is observed with increasing gap height, as can be seen in figure 3(*b*). Here, the collapse occurs on the upper boundary after a more prominent bubble expansion along the lower boundary. Although the bubble collapses onto the upper boundary, the upper wall of the bubble at its maximum size may or may not come into contact with it. When $0.4 < \eta < 0.8$, the bubble is able to

https://doi.org/10.1017/jfm.2011.212 Published online by Cambridge University Press

reach the upper wall at maximum expansion, as seen in frame 3 of figure 3(*b*). In the range $0.8 \leqslant \eta < 1.0$, however, the bubble expands but it does not reach the upper wall, see frame 3 of figure 3(*c*), i.e. it cannot drain out all the liquid in the gap and attains an oblate shape, $R_y/R_x = 0.84$, with a flat upper wall. Thus, at maximum expansion, a thin layer of liquid can be observed between the top of the bubble and the upper wall. The flat upper part of the bubble does not move inwards during the collapse; on the contrary, it is pushed up during the bubble contraction due to the inward motion of the lateral bubble walls; as the bubble collapse progresses the lower part of the bubble accelerates, causing the bubble centroid to move upwards ($t = 40.0\,\mu$s, figure 3*c*). Later, we expect the formation of a jetting flow between $t = 50.0\,\mu$s and $t = 53.3\,\mu$s. Nonetheless, a lower bound of the velocity can be estimated as the bubble detaches from the lower wall and impacts onto the upper wall; covering a distance of 130 μm in 3.3 μs gives a liquid speed of at least $40\,\mathrm{m\,s^{-1}}$.

3.2.3. *Neutral collapse*

For $1.0 < \eta < 1.4$, the upper part of the bubble does not come any longer in contact with the upper wall, see figure 3(*d*), $\eta = 1.2$, and the collapse proceeds within the gap, similar to the disk-shaped bubble which also collapses in this fashion. Also, in this region when the bubble reaches its maximum expansion, $R_y/R_x = 0.96$; thus the bubble is slightly oblate. The shape of the bubble resembles the elliptical shapes recently studied by Lim *et al.* (2010), except that this bubble is only half an ellipse due to the presence of the solid wall. During the contraction of the bubble the ellipse's axis inversion is observed, the lateral sides of the bubble move inwards faster than the less curved upper wall of the bubble (frame 4 at $t = 33.3\,\mu$s); thus they move the upper wall slightly upwards. As the bubble continues to contract, it becomes slender and in frame 5, $t = 43.3\,\mu$s, its shape already displays a longer vertical axis than its horizontal axis; the contraction is so fast that an exposure time of 1 μs depicts this bubble motion blurred (frame 5). At the moment of collapse, the bubble's lateral walls may split the bubble into two parts, as seen in the numerical simulations of Lim *et al.* (2010). Frame 6 shows the bubble during its very late stage of collapse. We think that the lower more fuzzy part has already collapsed while the upper part is just about to reach its minimum volume. Interestingly, numerical simulations performed by Borkent *et al.* (2009) of a single bubble collapsing in a crevice resemble the collapse of this bubble. They noted the split of the bubble followed by two fast jets moving in opposite directions. If this same mechanism occurs in figure 3(*d*) between frames 5 and 6, a fast and narrow jet would pierce through the bubble and impact on the lower boundary. In the last frame, the bubble content has condensed back into the liquid.

3.2.4. *Collapse onto the lower wall*

The collapse onto the lower wall consists of two sub-regions, the first one occurs for $1.4 < \eta < 7.0$, where the bubble dynamics are affected by the upper wall and the bubble acquires a quasi-conical shape during the collapse; see frames 5 and 6 in figure 3(*e*). The bubble reaches its maximum expansion with $R_y/R_x = 0.97$; thus, the bubble shape is slightly oblate. The lateral side of the bubble having a larger curvature starts to collapse faster than the upper part having a smaller curvature; however, the solid boundary hinders the flow of the lower part of the bubble and thus the bubble acquires a quasi-conical shape ($t = 30\,\mu$s); with this shape the contraction of the bubble proceeds having as its main accelerating mechanism the involution of the now more curved upper bubble wall (see Philipp & Lauterborn 1998, their figure 2(*h*) for stand-off distance $\gamma = 0.6$). The inward-directed flow into a volume becoming smaller

https://doi.org/10.1017/jfm.2011.212 Published online by Cambridge University Press

and smaller accelerates the bubble surface as long as it is curved convexly (Lauterborn 1982; Vogel *et al.* 1989). Since nothing retards the motion of the upper wall of the bubble, it may develop a jet at a late stage of its collapse. Yet, in the experiments conducted here in this regime between $1.4 < \eta < 7.0$ no jet could be resolved, which we attribute to the insufficient spatial and temporal resolution. Similarly, Philipp & Lauterborn (1998) did not observe a jet at a stand-off distance $\gamma = 0.1$, which also may be due to the limited number of frames and difficulties of visualization.

3.2.5. *Quasi-hemispherical collapse*

The second sub-region for bubbles collapsing on the lower wall occurs for $\eta > 7.0$. The images of the cavitation bubbles in this region are depicted in figure 3(*f*). When the upper wall is far away the bubble no longer experiences the presence of the upper wall and attains an almost perfect hemispherical shape, $R_y/R_x = 0.99$, as seen in frame 3; thus, the change in the shape of the bubble is not as pronounced as in the cases of lower η. Even though the bubble appears to collapse spherically it does not, because the upper wall of the bubble moves faster than the lateral walls; the aspect ratio, $R_y(t)/R_x(t)$, in frames 3, 4, 5 and 6 is 0.99, 0.92, 0.82 and 0.52, respectively. It has already been discussed by Lauteborn (1982) and Vogel *et al.* (1989) that more highly curved parts of an elongated bubble corresponding to a smaller bubble collapse faster than the less curved parts. This is true for all the cases studied; however, the case of $\eta > 7.0$ is of particular interest because the bubble starts from an almost spherical shape, $R_y/R_x = 0.99$; thus, the curvature of the bubble is uniform everywhere. Nevertheless, the lower part of the bubble in contact with the solid boundary retards the motion of the lateral walls as compared to the upper wall, thus creating the change in the aspect ratio observed during the bubble collapse (this has also been observed by Philipp & Lauterborn 1988). This might be due to the fact that the bubble is not initiated exactly at the boundary, and viscous boundary layers or the solid–liquid contact may also play a role. In this regime, for $\eta > 7$, no jet onto the lower wall was observed either. A jet might have occurred, but the frame rate is too low for such a jet to be observed.

3.3. *Volume dynamics*

Figure 4 shows four plots of $R_{eq}(t)$ as a function of time for selected η values and same laser energy; R_{eq} is the equivalent radius defined as the radius of a hemisphere with the same volume of the cavity. The bubble's equivalent radius, $R_{eq}(t)$, was calculated from the captured images; first, the boundary of the bubble was located as shown in the inset of figure 4, then it was treated as if it consisted of thin disks of height dh equal to the size of each pixel; the summation of the volumes of the thin disks yields the total volume of the hemispherical bubble from where the equivalent radius is obtained. The first experimental value that corresponds to the first image of the bubble taken during its expansion has a larger experimental error. This is due to the rapid expansion of the bubble such that the images are slightly blurred. Also, the last frame before the bubble disappears shows a very fast collapse of the bubble; therefore; its experimental error is larger too.

Figure 4 demonstrates that the expansion and collapse phases are not symmetric with a clearly faster growth phase initiated at $t = 0$. The asymmetry between the expansion and collapse phases has been observed earlier, see for instance (Chen, Chu & I 2006; Zwaan *et al.* 2007). For $\eta = 0.4$ the collapse period is almost 10 µs larger than the expansion phase. This difference reduces to a few microseconds for larger η values. We have no clear evidence of the cause of this asymmetry in the

https://doi.org/10.1017/jfm.2011.212 Published online by Cambridge University Press

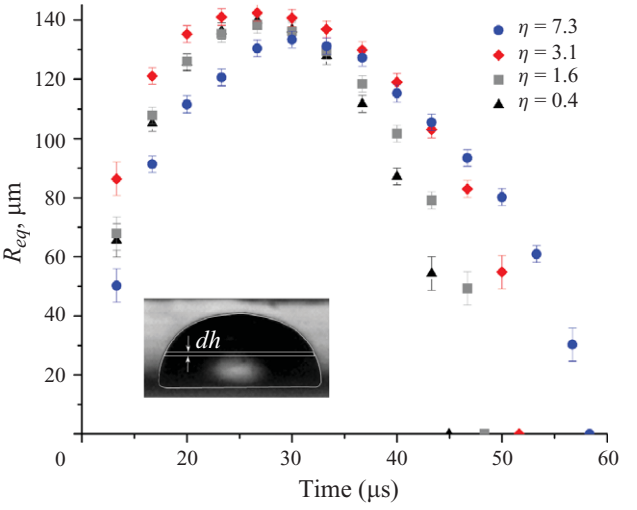


FIGURE 4. (Colour online) The dynamics of the equivalent bubble radius for varying wall positions, η, and the same laser energy. Note that the expansion phase is shorter than the collapse phase for increasing η values. The inset depicts the geometry to obtain R_{eq} from a solid of revolution integral with steps dh using image processing routines.

dynamics. Indeed, viscous effects have an impact as η decreases. The fast expansion may also be due to a high vapour pressure initially, which reduces as the bubble interior cools down during expansion (Zwaan *et al.* 2007). Yet, this may not explain the effect of η on the asymmetry. Lastly, elasticity of the walls may affect the bubble dynamics becoming more important as less liquid is available. More recently, Sun *et al.* (2009) have shown that thermal effects play an important role in confined geometries.

Figure 5 shows the results of 90 experimental runs performed. The curve $\beta = 1/\eta$ represents the curve for a hemispherical bubble with $R_x = R_y$. Four different bubble size regimes were tested by setting the energy of the laser to four distinct values. Because of fluctuations in the laser energy, variations in the maximum radius (for each energy setting) of the hemispherical bubbles of approximately $\pm 4\,\%$ were observed. Figure 5 therefore uses the averaged R_x for each energy setting. In the experiments performed the bubble size ranged from 80 to 170 µm, so w/R_x (see figure 1) ranged from 3.6 to 7.5. While the bubble dynamics may be affected by the proximity of the front and back walls, the experimental results show the same bubble dynamics for the different size of bubbles tested, as seen in figure 2.

Figure 6 is a close-up of the region $0 < \eta \leqslant 2$. Here, four different regions were observed, disk-shaped collapse, upward jetting, neutral collapse and non-spherical collapse with a conical shape onto the lower wall. Images that show the final shape of the bubble before it vanishes are also shown in figure 6. The grey vertical lines denote the transition region between the different regimes. When the gap between the walls is sufficiently small the upper pole of the bubble is able to make contact with the upper wall so that the maximum vertical expansion is limited. In this situation the ratio of R_y to H, $\beta = 1$. Yet, figure 6 reveals that for $0.7 < \eta < 1$ the bubble does not reach the upper wall and attains an oblate shape. The experimental results depart from the hemispherical curve for $\eta \leqslant 1.8$. For $\eta > 1.8$, the experimental values follow the $\beta = 1/\eta$ curve fairly accurately. In the range $0 < \eta \leqslant 1.8$ the bubble dynamics changes drastically, giving rise to the different bubble collapse regimes just mentioned.

https://doi.org/10.1017/jfm.2011.212 Published online by Cambridge University Press

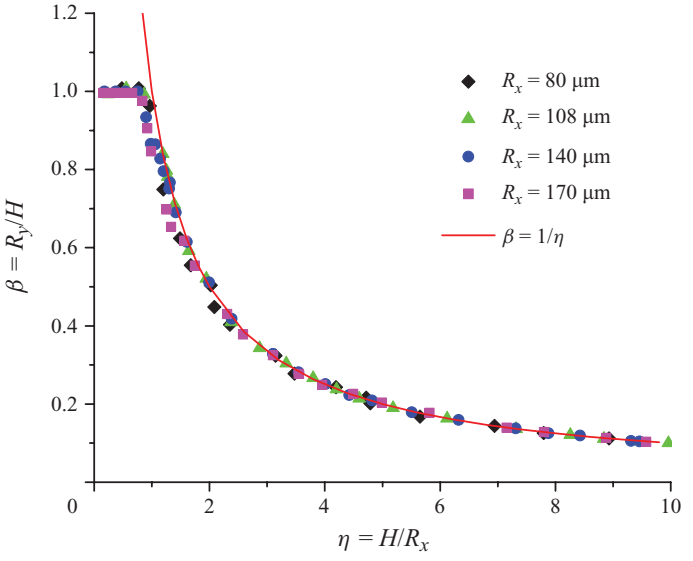


FIGURE 5. (Colour online) Graph of the non-dimensional bubble to channel height ratio $\beta = R_y/H$, as a function of the non-dimensional channel height, $\eta = H/R_x$. The solid line depicts the limit of a hemispherical bubble.

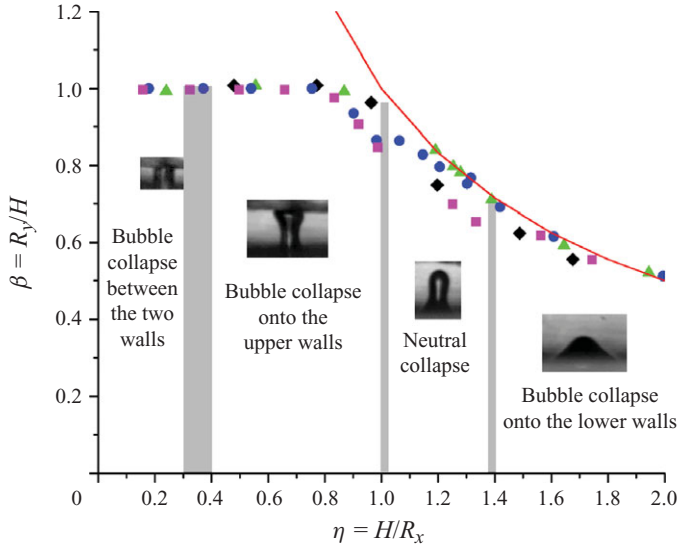


FIGURE 6. (Colour online) Expanded view of figure 5 for small non-dimensional channel heights revealing the non-hemispherical dynamics with four different regimes of the bubble collapse.

4. Comparison of experiments with boundary element simulations

The experiments conducted show that the height of the channel strongly influences the bubble dynamics; the bubble collapse changes significantly in a very narrow range of η values. In addition to that, the final stage of the collapse occurs very fast and details of the final stage of the bubble collapse could not be observed. Due to the rapid evolution of the bubble collapse, numerical simulations were conducted to gain

https://doi.org/10.1017/jfm.2011.212 Published online by Cambridge University Press

further insight into the physics of bubbles collapsing between two plates separated at distance H. The comparison between experimental and numerical results is only shown from the bubble's maximum radius onwards; the simulated time, t', shown below each frame of Figure 7, is set to zero when the bubble reaches its maximum expansion. Simulation results from the initiation to maximum expansion are not shown here; however, figure 11 depicts one example of the complete cycle for $\eta = 1.5$ (please note that $t' = 0$ in figure 11 starts with the expansion phase). A brief explanation of the numerical method is given in the Appendix with further details available in the listed references. The numerical simulations are different from the experimental results in two aspects, the bubble position at the moment of inception and the geometry of the walls. First, the η values of the numerical simulations are slightly larger than those of their corresponding experimental values because the bubble is created at a distance of $0.5R_x$ from the lower wall instead of being created at the lower boundary. Placing the bubble too close to the lower boundary poses numerical difficulties. Second, the axisymmetric simulations assume that the bubble is created between two circular elements separated at distance H as opposed to be created in a rectangular geometry. In addition, viscous effects are not considered, which may become important as the distance between the plates is small enough such that vorticity diffusions affects the central flow; other effects that are not taken into account are the elasticity of the walls, shock waves and thermal effects. Sun *et al.* (2009) reported that incorporating heat transfer and viscous effects to a purely one-dimensional inertia-driven model can explain some features of their experimental results. Yet, here we emphasize on a simple potential flow model and compare bubble translation, bubble shape and the jet direction with the experiment.

Figure 7(*a–d*) shows frames that correspond to the collapse phase of the bubbles created between two walls for different η values. In each frame, the simulated time, t', in microseconds is shown. The frames shown start when the bubble reaches its maximum expansion, $t' = 0$, until the bubble breaks up into two or more parts or when the jet impacts onto one of the boundaries. The value of the bubble radius used in the simulations is the value of the bubble radius observed experimentally, in figure 7(*a–d*) $R_x = 140 \pm 4\,\mu$m. Although we find a slight discrepancy between the experimental and the simulated collapse times, the shapes agree surprisingly well; this discrepancy decreases with larger η values.

4.1. *Bubble collapse onto the upper wall*

Figure 7(*a*) shows the numerical results of $\eta = 1.5$; these results correspond to the experimental results of $\eta = 0.9$, see figure 3(*c*). The images of the upper row are numerical simulation results corresponding to the initial collapse phase of the bubble beginning with the bubble at maximum expansion; the experimental shape of the bubble at maximum expansion can be seen in the third frame from the left in figure 3(*c*). The images in the lower row correspond to the final stage of the bubble collapse. These images show the contour of the bubble with a dotted line to denote the stages of the bubble collapse that were not captured in the high-speed video. The upper and lower walls are indicated by solid lines. The experimental results show that at maximum expansion the bubble does not reach the upper wall, see the third frame from the left in figure 3(*c*), where the R_y/H ratio is 0.93. The bubble reaches the upper boundary later in the collapse phase; frame 4 of figure 3(*c*) shows the bubble with a flat upper wall in contact with the upper boundary. Interestingly, this characteristic is also shown in the numerical simulations, that is, at maximum expansion the movement of the bubble wall is not zero everywhere; in fact, the upper

https://doi.org/10.1017/jfm.2011.212 Published online by Cambridge University Press

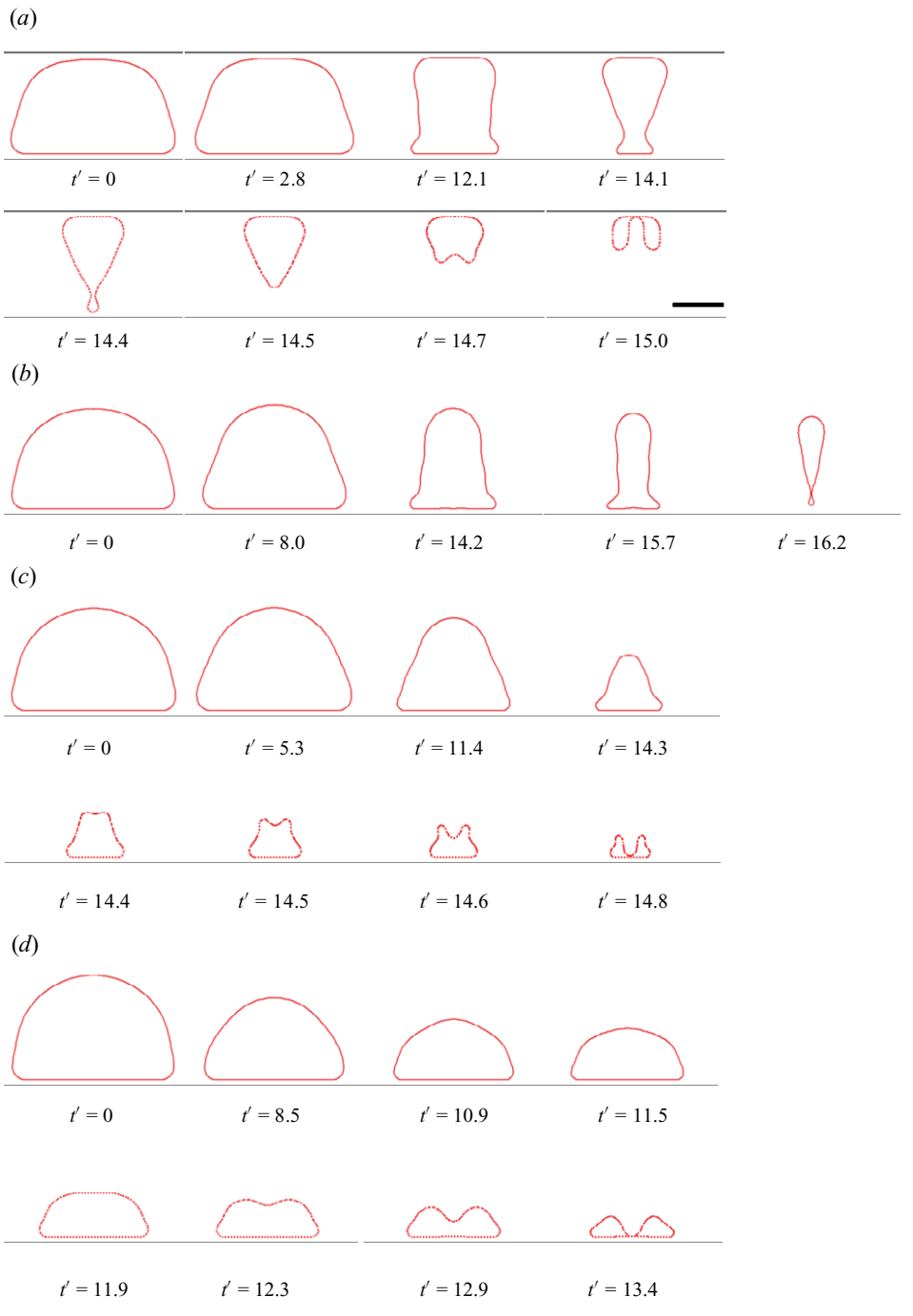


FIGURE 7. (Colour online) Numerical results of the collapse of a bubble with an approximate maximum horizontal radius of $R_x = 140\,\mu$m in a channel of varying height. The simulated time t', in microseconds, is shown below each image. The four simulated collapse scenarios are: (*a*) collapse with upward jetting, $\eta = 1.5$; (*b*) neutral collapse, $\eta = 1.75$; (*c*) non-spherical collapse onto the lower wall, $\eta = 2.0$; (*d*) quasi-hemispherical collapse onto the lower wall, $\eta = 7.0$. For all the simulations, the non-dimensional plate length is $L = 3$ and the stand-off parameter is $\gamma = 0.5$. The expansion phase is not shown. t' is set to zero at the maximum bubble size. The horizontal bar in the lower right corner of (*a*) depicts a length of 100 μm, which is applicable to (*b–d*).

https://doi.org/10.1017/jfm.2011.212 Published online by Cambridge University Press

part still expands while the lower part is already collapsing. In the first frame of the simulated bubbles, the R_y/H ratio is 0.93. During the collapse phase, the upper part of the bubble flattens as it reaches the upper wall with zero curvature. The collapse phase continues with the upper part of the bubble fixed to the upper solid wall. Frames 5 and 6 in figure 3(*c*) show the bubble in contact with the upper wall; frame 6 shows the bubble with its upper half larger than its lower half; the final stage of the bubble collapse is not captured. Frame 7 shows that the bubble has condensed back into the liquid. The simulated bubbles show similar dynamics; frames 2–4 of the upper row show similar shape as the experimental images. The lower row shows that when the lateral walls of the bubble move inwards the lower half tends to move faster, thus creating an inverted cone-like shape ($t' = 14.4\,\mu s$). The lower wall of the bubble detaches from the lower boundary and moves towards the upper wall piercing through itself.

Between the last image of the upper row and the first image of the lower row, the lower lateral walls of the bubble accelerate very rapidly while the upper wall of the bubble, which is flat, does not move inwards. The final stage of the bubble collapse takes place in 0.9 μs, which is shorter than the experimental inter-frame time of 3.3 μs.

4.2. *Neutral bubble collapse*

Figure 7(*b*) displays the numerical results of $\eta = 1.75$, the corresponding experimental values are those shown in figure 3(*d*) for $\eta = 1.2$ (experimentally $R_y/H = 0.8$ while numerically $R_y/H = 0.85$). When the bubble reaches its maximum expansion, see frame 3 of figure 3(*d*), a slightly oblate bubble ($R_y/R_x = 0.96$) is seen. During the collapse phase the bubble contracts very rapidly in the horizontal direction (becomes thinner), see frames 5 and 6 of figure 3(*d*), inverts its major axis and collapses at the centre of the channel (frame 7). The simulated bubble tends to become thinner, but no inversion of the axis is observed since the vertical axis of the bubble is slightly larger than the horizontal axis at the moment of maximum expansion. In the simulations, the bubble contracts rapidly in the horizontal direction, agreeing well with the experimental images. Moreover, the horizontal contraction of the bubble causes a split of the bubble into two. The difference between frames 4 and 5 of the simulated images occurs within 0.5 μs, which again is much shorter than the experimental inter-frame time of 3.3 μs.

4.3. *Non-spherical collapse onto the lower wall*

In figure 7(*c*) the numerical results of $\eta = 2.0$ are shown, which correspond to the experimental results of $\eta = 1.6$, see figure 3(*e*). At maximum expansion, the simulated bubble acquires a prolate shape while the experimental bubble displays an almost spherical shape (experimentally $R_y/H = 0.6$ and numerically $R_y/H = 0.8$). Qualitatively, the evolution of numerical images resembles the evolution of the experimental bubbles. The numerical solution displays a jet that develops at the final stage of the bubble collapse, shown in the lower row with the bubbles by a dotted line; the experimental images do not show a jet. According to the simulation, the jet only develops in the last phase of the bubble collapse. The first two simulation images show similar shapes as the frames 3 and 4 from the experiment, see figure 3(*e*); the width and the curvature of the bubble are similar. The bubble starts to collapse in a quasi-conical shape at $t = 36.7\,\mu s$, which is reproduced in the simulations, see frame 3 in figure 7(*c*). The simulations reveal a bubble collapse onto the lower wall and a jet that develops late and is resolved in the lower row of figure 7(*c*).

https://doi.org/10.1017/jfm.2011.212 Published online by Cambridge University Press

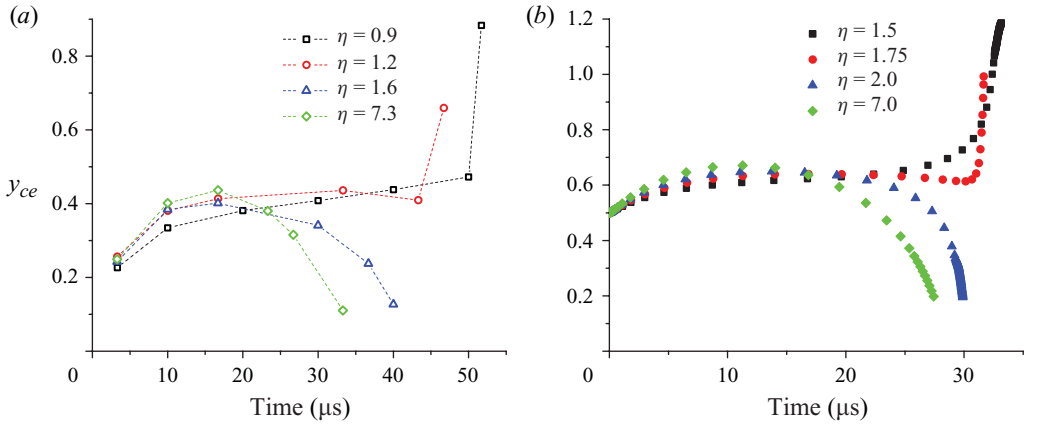


FIGURE 8. (Colour online) Experimentally (a) and numerically (b) determined centre of mass of the bubble as a function of time for four selected η values (0.9, 1.2, 1.6 and 7.3) demonstrating the motion of the bubble during expansion and collapse.

4.4. *Quasi hemispherical collapse onto the lower wall*

Figure 7(d) compares the numerical results of $\eta = 7.0$ with the experiment shown in figure 3(f) ($\eta = 7.3$, experimental $R_y/H = 0.1$ and numerical $R_y/H = 0.2$). In the third image of figure 3(f) the bubble reaches its maximum expansion almost like a perfect sphere, while during the collapse phase the bubble does no longer display the quasi-conical shape observed at lower η values; yet the upper wall of the bubble moves slightly faster than its lateral side. This may give rise to the formation of a jet which cannot be resolved experimentally. The simulations indeed reveal a jetting bubble in the very late stage, see the lower row of figure 7(d).

For the choices of the initial bubble position and size of the wall tested so far, the pronounced difference between the expansion and collapse phases (see figure 4) is not observed in the simulations. Therefore, we expect that this is caused by viscous effects, e.g. build-up of boundary layers and the flow reversal, the elasticity of the boundaries of the test section or thermal effects. All these effects are not accounted for in the potential flow model used.

4.5. *Centroid motion and Kelvin impulse*

Figures 3 and 7 demonstrate that the bubble direction of motion during collapse depends on the η value. We now substantiate the dynamics by measuring the bubble's centroid position and compare it with the simulation results. From the high-speed movies the centroid is determined from the vertical centre of mass assuming axisymmetry. Figure 8 compares both the normalized experimental, y_{ce}, and numerical positions, y_{cn}, of the bubble centroid. We find that during expansion the centroid of the bubble moves away from the lower boundary where it has been created. This behaviour is commonly observed for single bubble dynamics studies near boundaries (Benjamin & Ellis 1966; Blake & Gibson 1987).

During the collapse we find the aforementioned separation, i.e. for η values sufficiently large, the bubble moves towards the lower boundary while smaller values lead to a translation of the bubble centroid and collapse towards the upper surface.

Although there is a discrepancy of the absolute timings, the structure of the experimental curves (figure 8a) is in agreement with the simulation results. In particular, the acceleration of the bubble centroid is marked differently for the

https://doi.org/10.1017/jfm.2011.212 Published online by Cambridge University Press

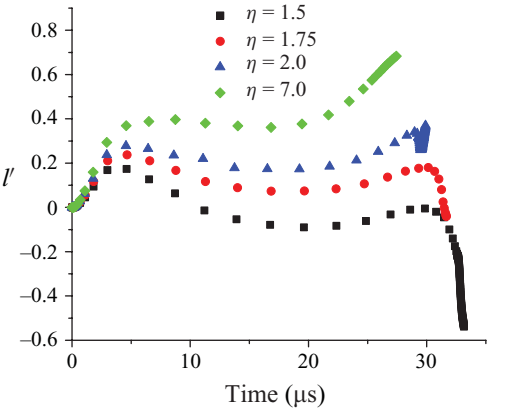


FIGURE 9. (Colour online) The temporal development of the Kelvin impulse obtained from the simulations (see text) is shown for the η values 0.9, 1.2, 1.6 and 7.3.

upward and downward motions. The collapse progresses quicker towards the upper gap wall, thus away from the location of nucleation, while the collapse for large η values is smoother.

Next, we evaluate the Kelvin impulse of the bubbles shown in figure 7; the Kelvin impulse is a useful tool to distinguish between radial symmetric bubble dynamics and non-spherical symmetric behaviour (usually jetting); it is a concept in bubble dynamics defined by Benjamin & Ellis (1966) and Blake & Gibson (1987) as

$$I = \rho \int_S \phi \boldsymbol{n}\, \mathrm{d}s, \tag{4.1}$$

where S is the surface of the bubble. A purely radial oscillating bubble has a zero Kelvin impulse, because $\int_S \boldsymbol{n}\, \mathrm{d}s = 0$ (the potential is the same everywhere on the bubble surface). On the other hand, a jetting bubble possesses a non-zero Kelvin impulse. In figure 9, the dimensionless Kelvin impulse I' is plotted ($I = I' R_x^3 \sqrt{\rho p_{ref}}$, see Klaseboer *et al.* 2007, with $p_{ref} = 1$ bar). In our case, the normal vector $\boldsymbol{n}$ is defined out of the fluid domain (into the bubble). During the collapse phase, the jet region exhibits a very strong negative potential. This results in a positive Kelvin impulse when the jet is directed towards the lower boundary and a negative Kelvin impulse when the jet is directed towards the upper boundary. Thus, the sign of the Kelvin impulse is opposite to the jetting motion due to the convention of the direction of the normal vector.

In figure 9, the Kelvin impulse as a function of time is plotted for the four bubbles of figure 7. All bubbles initially have an increasing Kelvin impulse for $t < 3\,\mu$s. A clear separation then occurs for the different η values. For the bubble with $\eta = 1.5$, the Kelvin impulse decreases and becomes negative around $t = 10\,\mu$s. During the jet formation, the Kelvin impulse reaches strongly negative values, corresponding to the upward jetting as observed in figure 7(*a*). The bubble with $\eta = 1.75$ has a Kelvin impulse around zero, corresponding to the neutral collapse (figure 7*b*). For the bubble with $\eta = 2.0$, the Kelvin impulse first decreases, but then increases again. This corresponds to the downward jetting observed in figure 7(*c*). Finally, the bubble with $\eta = 7.0$ has a Kelvin impulse that flattens but then grows again for $t > 20\,\mu$s. Thus, figure 9 clearly reveals the behaviour of the bubble; in general, the higher the value of η, the higher will be the Kelvin impulse.

https://doi.org/10.1017/jfm.2011.212 Published online by Cambridge University Press

5. Discussions and conclusions

The results presented here may be useful for evaluating the erosion mechanism in thin films, i.e. in bearings. Journal bearings and gears, among other mechanical elements, present a converging and a divergent section filled with a thin lubricating liquid film. In the converging section, the liquid pressure rises to values higher than the ambient pressure but at the divergent section the liquid experiences negative pressures, which may lead to cavitation (Dowson & Taylor 1979). In the divergent section, since the liquid height varies, different collapse scenarios may be present. In a recent study by Kasolang & Dwyer-Joyce (2008), the film thickness profile of a journal bearing was measured by means of ultrasound. The measurements were carried along the circumference of the bearing. They found cavitation to occur in the diverging section of the bearing covering an arc of approximately 20–30°. However, their results do not include information regarding the morphology or the collapse of cavities inside the liquid film.

Philipp & Lauterborn (1988) found strong evidence that suggests that the cause of erosion is the shock wave emitted when a bubble reaches its minimum volume. It may be possible to perform experiments in a thin gap when the bubble collapses between the two boundaries, i.e. $1.0 < \eta < 1.4$. Since the distance from the position at which the bubble reaches its minimum volume (the origin of the bubble-collapse shock wave) to the solid boundary, d, is small, the pressure acting on the boundary is high. Then, shock wave-induced damage can be evaluated on the upper boundary since no jet impinges on it.

Our work bridges the gap between the cavitation dynamics in very thin liquid gaps studied by Israelachvili's group (Chen & Israelachvili 1991 and You, Kuhl & Israelachvili 1992) and the semi-infinite domain. There, they use a surface force apparatus to reveal the importance of the explosive growth in nanometre thick films rather than the collapse. Due to the very thin films the fluid mechanics is viscosity dominated, thus slowing down or completely hindering the collapse. Yet, the expansion of the cavity is governed by the tensile stress, which ultimately cracks the liquid and nucleates an explosively expanding vapour cavity. Typical heights of the vapour cavities reported by You *et al.* (1992) are 100 nm, while in our current work the smallest cavities have a height of 30 μm, leading to a mainly inertia-dominated regime.

In summary, we studied the dynamics of laser-induced cavitation bubbles generated close to the lower surface in a gap composed of two rigid boundaries. We revealed novel dynamical features: the bubble shape and the collapse scenario depend on the non-dimensional gap height, which is the ratio between the liquid height and the maximum horizontal bubble radius. At low gap heights, the bubble collapses between the solid boundaries; however, with increasing gap heights the collapse position moves towards the upper boundary, and then again between the boundaries, and finally onto the lower boundary. The simulations based on a potential flow theory reveal the formation of rapid liquid jets, which may contribute to cavitation erosion in thin liquid films.

Appendix. The numerical model based on the boundary element method

The numerical simulations were performed with an axisymmetric boundary element method based on potential flow theory. A Reynolds number based on the gap height h and averaged jet velocity u_{jet} is given by $Re = hu_{jet}/\nu$; u_{jet} is a lower bound of the averaged impact jet velocity. It is assumed that the jet develops during the bubble

https://doi.org/10.1017/jfm.2011.212 Published online by Cambridge University Press

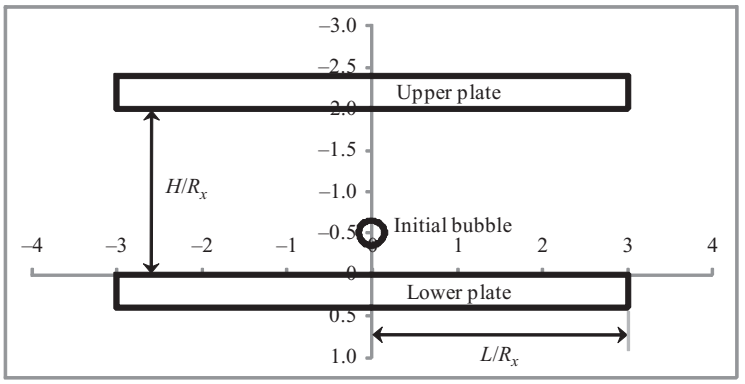


FIGURE 10. Mesh used for the numerical simulations (axial symmetric configuration). The bubble is initially placed at 0.5 times its maximum radius from the lower plate. The upper plate is placed at a distance H from the lower plate (here $H/R_x = 2$). The radius of both plates is $L/R_x = 3$ for this particular example. In this graph all lengths have been non-dimensionalized with R_x. The bubble will reach a maximum radius of about 1.0.

collapse from its maximum radius R_x; thus, $u_{jet} = R_x/t_c$. The simulated test of $\eta = 1.5$ corresponds to the experimental test of figure 3(*c*), the test with the smallest gap height of $h = 125\,\mu\text{m}$, $R_x = 140\,\mu\text{m}$, $t_c = 32\,\mu\text{s}$ and $\nu = 1.61 \times 10^{-6}\,\text{m}^2\,\text{s}^{-1}$. With these values $Re = 340$. Therefore, liquid inertia is important and in a good range for the potential flow approximation. Although the experimental set-up is not exactly axial symmetric, it is deemed to be a good first approximation of the physics involved. The boundary integral method makes use of the fact that the Laplace equation ($\nabla^2\phi = 0$) for the velocity potential $\boldsymbol{u} = \nabla\phi$ can be written as a surface integral using the Green function G as

$$c\phi + \int_S \phi \frac{\partial G}{\partial n}\,\mathrm{d}S = \int_S G \frac{\partial \phi}{\partial n}\,\mathrm{d}S, \tag{A 1}$$

where S is the surface of the problem and consists of three parts in this work, the lower solid surface, the upper solid surface and the bubble surface. Here, c is the solid angle on S and $\partial/\partial n = \underline{\boldsymbol{n}} \cdot \nabla$ represents the normal derivative on the surface S and thus $\partial\phi/\partial n$ is the normal velocity. In figure 10, the initial simulation conditions are shown for a typical case with plate radius $L = 3$. On the solid top and bottom surfaces, the conditions $\partial\phi/\partial n = 0$ are imposed. On the bubble surface, the potential is updated at each time step using the Bernoulli equation by setting the pressure just outside the bubble surface equal to the pressure inside the bubble (p_g, where surface tension has been neglected) as

$$\rho \frac{\mathrm{D}\phi}{\mathrm{D}t} = p_0 + \frac{\rho}{2}|\nabla\phi|^2 - p_g. \tag{A 2}$$

The material derivative used is defined as $\mathrm{D}/\mathrm{D}t = \partial/\partial t + \boldsymbol{u} \cdot \nabla$ since the bubble follows the flow. The density of the fluid is denoted by ρ. Equation (A 2) is discretized with time to get the potential on the bubble surface for the next time step (the right-hand side of this equation is assumed to be known from the previous time step). The pressure inside the bubble follows an adiabatic law as $p_g = p_{g0}(V_0/V)^\kappa$, with $p_{g0} = 100$ bar is the initial pressure of the bubble contents ($p_0 = 1$ bar is the reference pressure) and $\kappa = 1.25$ is the ratio of specific heats taken to be similar as the value for an explosion bubble (see Cole 1948; Lee, Klaseboer & Khoo *et al.* 2007). Here V and

https://doi.org/10.1017/jfm.2011.212 Published online by Cambridge University Press

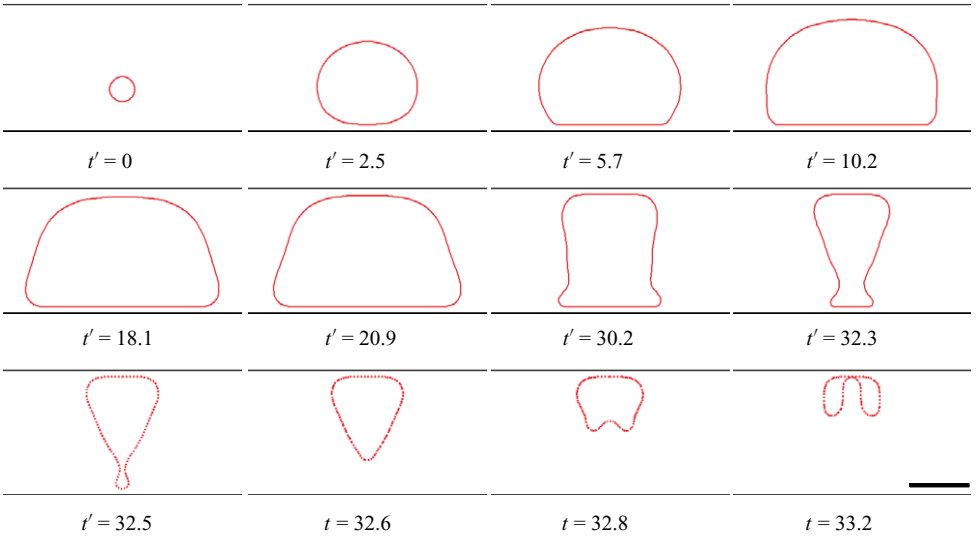


FIGURE 11. (Colour online) Example of the expansion and collapse dynamics of a bubble in a narrow gap, $\eta = 1.5$. The solid bar on the lower right corner indicates a length of 100 μm.

V_0 are the volume and the initial volume of the bubble, respectively (the initial radius of the bubble is chosen to be 0.1485 times the maximum bubble radius in order to get a maximum dimensionless bubble radius of about 1.0). The numerical results do not seem to depend much on the exact value of p_{g0}. The bubble position is updated with the velocity vector $\boldsymbol{u}$ at each time step. The velocity vector can be constructed with the normal velocity $\partial\phi/\partial n$ and the tangential velocity, which in turn is obtained from the distribution of the potential on the bubble surface. The mesh is divided into 51 nodes on the bubble, 25 on the lower surface and 26 on the upper surface. The thickness of the plates is chosen to be $0.4R_x$ (see figure 10). Both the length L and distance between the plates H can be varied. The boundary element equation then provides a system of equations which can be solved for the unknown normal velocity on the bubble surface. The simulations are continued until the bubble breaks up into multiple parts, or until jet impact occurs. In order to prevent numerical instabilities due to the close proximity of the bubble with the plate, the bubble is not allowed to approach either plate less than $0.075R_x$. The film thickness value of $0.075R_x$ was carefully selected as it should roughly be of the same length as the distance between the nodes on the solid. On the solid, the nodes are more sparsely distributed. A too close distance will cause numerical instabilities, and a too large distance will create an unnecessary thick film, which will influence the results. By evaluating several values of the film thickness, we found that the value $0.075R_x$ is the optimum value between accuracy and robustness. The potential in this 'film area' is set to a constant equal to the potential just outside the film. For more information concerning the numerical details, the reader is referred to Wang *et al.* (1996).

Figure 11 shows both the expansion and collapse phases of a simulated bubble and the position at which the bubble starts to expand. Figure 12 shows the dependence of the oscillation time as a function of H and L. In order to be able to compare the results, the oscillation time and plate radius are given non-dimensionalized. In this way, a freely oscillating bubble (spherical, no nearby boundaries) will oscillate with a period of $t_{osc} = 1.998$ in units of $R_x\sqrt{\rho/p_0}$ (see figure 12). The difference as compared

https://doi.org/10.1017/jfm.2011.212 Published online by Cambridge University Press

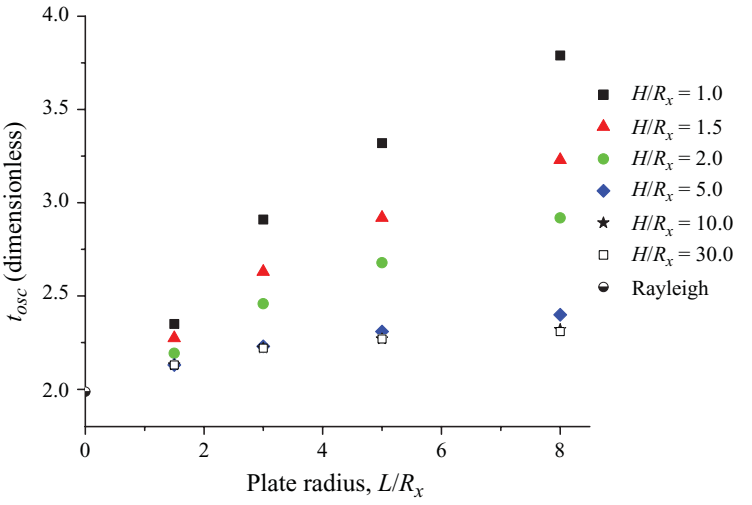


FIGURE 12. (Colour online) Dimensionless collapse time as a function of plate radius L/R_x and gap size H/R_x. For small gap sizes ($H/R_x = 1$), the collapse time increases almost linearly with the plate radius. For larger gap sizes ($H/R_x = 30$), the collapse time becomes independent of L/R_x, indicating that the upper plate does no longer influence the behaviour of the bubble; thus, the bubble is basically oscillating near one solid wall only. Time is made non-dimensionless with $R_x\sqrt{\rho/p_0}$ and the plate radius with R_x.

to two times the Rayleigh collapse time, e.g. $t_{osc} = 1.83$, is due to the modelling of the bubble content as an isotropic gas and the distinct initial conditions. For a very small inter-plate distance ($H/R_x = 1$), the oscillation time increases almost linearly with the plate radius. For larger inter-plate distances, the oscillation time approaches a constant value. The difference in oscillation time between $H/R_x = 10$ and 30 is quite minimal. This indicates that the bubble does no longer 'feel' the second plate and essentially oscillates as if it was placed in a semi-infinite space (i.e. a bubble near an infinite solid wall). It is well known that the oscillation time for a bubble near a plate is higher than that for a free field bubble (Vogel & Lauterborn 1988).

REFERENCES

BENJAMIN, T. B. & ELLIS, A. T. 1966 Collapse of cavitation bubbles and pressure thereby produced against solid boundaries. *Phil. Trans. R. Soc. Lond.* A **260**, 221–240.

BLAKE, J. R. & GIBSON, D. C. 1987 Cavitation bubbles near boundaries. *Annu. Rev. Fluid Mech.* **19**, 99–123.

BORKENT, B. M., GEKLE, S., PROSPERETTI, A. & LOHSE, D. 2009 Nucleation threshold and deactivation mechanisms of nanoscopic cavitation nuclei. *Phys. Fluids* **21**, 102003.

CHAHINE, G. L. 1982 Experimental and asymptotic study of non-spherical bubble collapse. *Appl. Sci. Res.* **38**, 187–197.

CHEN, Y. H., CHU, H. Y. & I, L. 2006 Interaction and fragmentation of pulsed laser induced microbubbles in a narrow gap. *Phys. Rev. Lett.* **96**, 034505.

CHEN, Y. L. & ISRAELACHVILI, J. 1991 New mechanism of cavitation damage. *Science* **252**, 1157–1160.

COLE, R. H. 1948 *Underwater Explosions*. Princeton University Press.

DIJKINK, R. & OHL, C. D. 2008 Laser-induced cavitation based micropump. *Lab on a Chip* **8**, 1676–1681.

DOWSON, D. & TAYLOR, C. M. 1979 Cavitation in bearings. *Annu. Rev. Fluid Mech.* **11**, 35–66.

https://doi.org/10.1017/jfm.2011.212 Published online by Cambridge University Press

Ishida, H., Nuntadusit, C., Kimoto, H., Nakagawa, T. & Yamamoto, T. 2001 Cavitation bubble behavior near solid boundaries. In *CAV 2001: Fourth Intl Symp. on Cavitation, 20–23 June 2001, California Institute of Technology, Pasadena, CA, USA* (CAV2001:sessionA5.003).

Kasolang, S. & Dwyer-Joyce, R. S. 2008 Observations of film thickness profile and cavitation around a journal bearing circumference. *Tribol. Trans.* **51**, 231–242.

Kim, W., Kim, T. H., Choi, J. & Kim, H. Y. 2009 Mechanism of particle removal by megasonic waves. *Appl. Phys. Lett.* **94**, 081908.

Klaseboer, E., Fong, S. W., Turangan, C. K., Khoo, B. C., Szeri, A. J., Calvisi, M. L., Sankin, G. N. & Zhong, P. 2007 Interaction of lithotripter shockwaves with single inertial cavitation bubbles. *J. Fluid Mech.* **593**, 33–56.

Krefting, D., Mettin, R. & Lauterborn, W. 2004 High-speed observation of acoustic cavitation erosion in multibubble systems. *Ultrason. Sonochem.* **11**, 119–123.

Kucherenko V. V. & Shamko, V. V. 1986 Dynamics of electric-explosion cavities between two solid parallel walls. *J. Appl. Mech. Tech. Phys.* **27**, 112–115.

Lauterborn, W. 1982 Cavitation bubble dynamics – new tools for an intricate problem. *Appl. Sci. Res.* **38**, 165–178.

Le Gac, S., Zwaan, E., Van Den Berg, A. & Ohl, C. D. 2007 Sonoporation of suspension cells with a single cavitation bubble in a microfluidic confinement. *Lab on a Chip* **7**, 1666–1672.

Lee, M., Klaseboer, E. & Khoo, B. C. 2007 On the boundary integral method for the rebounding bubble. *J. Fluid Mech.* **570**, 407–429.

Lindau, O. & Lauterborn, W. 2003 Cinematographic observation of the collapse and rebound of a laser-produced cavitation bubble near a wall. *J. Fluid Mech.* **479**, 327–348.

Lim, K. Y., Quinto-SU, P. A., Klaseboer, E., Khoo, B. C., Venugopalan, V. & Ohl, C. D. 2010 Nonspherical laser-induced cavitation bubbles. *Phys. Rev.* E **81**, 016308.

Ohl, C. D., Arora, M., Ikink, R., De Jong, N., Versluis, M., Delius, M. & Lohse, D. 2006 Sonoporation from jetting cavitation bubbles. *Biophys. J.* **91**, 4285–4295.

Philipp, A. & Lauterborn, W. 1998 Cavitation erosion by single laser-produced bubbles. *J. Fluid Mech.* **361**, 75–116.

Quinto-Su, P. A., Huang, X. H., Gonzalez-Avila, S. R., Wu, T. & Ohl, C. D. 2010 Manipulation and microrheology of carbon nanotubes with laser-induced cavitation bubbles. *Phys. Rev. Lett.* **104**, 014501.

Quinto-Su, P. A., Lim, K. Y. & Ohl, C. D. 2009 Cavitation bubble dynamics in microfluidic gaps of variable height. *Phys. Rev.* E **80**, 047301.

Reynolds, O. 1886 On the theory of lubrication and its applications to Mr Beauchamp's experiments, including an experimental determination of the viscosity of olive oil. Reprinted from the *Phil. Trans. R. Soc.*, Part I; see also Papers on Mechanical and Physical Subjects, Cambridge University Press, Volume II, 1901 for a reprint.

Shima, A. & Nakajima, K. 1977 Collapse of a non-hemispherical bubble attached to a solid wall. *J. Fluid Mech.* **80**, 369–391.

Sun, C., Can, E., Dijkink, R., Lohse, D. & Prosperetti, A. 2009 Growth and collapse of a vapour bubble in a microtube: the role of thermal effects. *J. Fluid Mech.* **632**, 5–16.

Tong, R. P., Schiffers, W. P., Shaw, S. J., Blake, J. R. & Emmony, D. C. 1999 The role of 'splashing' in the collapse of a laser-generated cavity near a rigid boundary. *J. Fluid Mech.* **380**, 339–361.

Vogel, A. & Lauterborn, W. 1988 Acoustic transient generation by laser-produced cavitation bubbles near solid boundaries. *J. Acoust. Soc. Am.* **84**, 719–731.

Vogel, A., Lauterborn, W. & Timm, R. 1989 Optical and acoustic investigations of the dynamics of laser-produced cavitation bubbles near a solid boundary. *J. Fluid Mech.* **206**, 299–338.

Wang, Q. X., Yeo, K. S., Khoo, B. C. & Lam, K. Y. 1996 Nonlinear interaction between gas bubble and free surface. *Comput. Fluids* **25**, 607–628.

You, L. C., Kuhl, T. & Israelachvili, J. 1992. Mechanism of cavitation damage in thin liquid-films-collapse-damage vs inception damage. *Wear* **153**, 31–51.

Zwaan, E., Le Gac, S., Tsuji, K. & Ohl, C. D. 2007 Controlled cavitation in microfluidic systems. *Phys. Rev. Lett.* **98**, 254501.

https://doi.org/10.1017/jfm.2011.212 Published online by Cambridge University Press